Journal of Power Sources 509 (2021) 230345

Contents lists available at ScienceDirect

Journal of Power Sources

journal homepage: www.elsevier.com/locate/jpowsour

Overpotential analysis of graphite-based Li-ion batteries seen from a porous electrode modeling perspective

Zhiqiang Chen [a,b], Dmitri L. Danilov [a,b], Luc H.J. Raijmakers [b], Kudakwashe Chayambuka [a,b], Ming Jiang [a,b], Lei Zhou [a,b], Jiang Zhou [c], Rüdiger-A. Eichel [b,d], Peter H.L. Notten [a,b,e,*]

[a] Eindhoven University of Technology, Eindhoven, 5600 MB, the Netherlands
[b] Fundamental Electrochemistry (IEK-9), Forschungszentrum Jülich, D-52425, Germany
[c] Tianjin Lishen Battery Joint-stock Co., Ltd, Tianjin, 300384, China
[d] RWTH Aachen University, D-52074, Aachen, Germany
[e] University of Technology Sydney, Broadway, Sydney, NSW, 2007, Australia

HIGHLIGHTS

- Analytical overpotential expressions are derived from P2D model.
- Four overpotential components contribute to the total battery overpotential.
- Four overpotential components are coupled together by the reaction rate distribution.
- Fluctuations in overpotential components are related to the reaction rate distribution.

ARTICLE INFO

Keywords:
Overpotential
P2D model
Reaction-rate distribution
Porous electrodes
Li-ion batteries

ABSTRACT

The overpotential of Li-ion batteries is one of the most relevant characteristics influencing the power and energy densities of these battery systems. However, the intrinsic complexity and multi-influencing factors make it challenging to analyze the overpotential precisely. To decompose the total overpotential of a battery into various individual components, a pseudo-two-dimensional (P2D) model has been adopted and used for electrochemical simulations of a graphite-based porous electrode/Li battery. Analytical expressions for the total overpotential have been mathematically derived and split up into four terms, associated with the electrolyte concentration overpotential, the Li concentration overpotential in the solid, the kinetic overpotential, and the ohmic overpotential. All these four terms have been separately analyzed and are found to be strongly dependent on the physical/chemical battery parameters and the reaction-rate distribution inside the porous electrode. The reaction-rate distribution of the porous electrode is generally non-uniform and shows dynamic changes during (dis)charging, resulting in fluctuations in the four overpotential components. In addition, the disappearance of the phase-change information in the voltage curve of the graphite-based porous electrode/Li battery under moderate and high C-rates is ascribed to the Li concentration overpotential among solid particles, resulting from the non-uniform reaction-rate distribution.

1. Introduction

Li-ion batteries (LIB) have been successfully applied in portable electronic devices, electric vehicles (EV), and hybrid electric vehicles (HEV) due to their high energy and power density, high coulombic and energy efficiency, and low cost [1]. For EV and HEV applications, the power density is expected to be high to meet the dynamic power requirements under real-life driving conditions. However, the internal battery resistance generates an overpotential, leading to an additional change in the battery voltage during operation. The resulting overpotential will inevitably decrease the useable power and energy densities, shortening the operating time of LIB. In addition, large overpotentials resulting from high resistances will induce intensive heat generation, causing major safety problems [2]. Hence, focusing on the

* Corresponding author. Eindhoven University of Technology, Eindhoven, 5600 MB, the Netherlands.
E-mail address: p.h.l.notten@tue.nl (P.H.L. Notten).

https://doi.org/10.1016/j.jpowsour.2021.230345
Received 10 May 2021; Received in revised form 16 July 2021; Accepted 1 August 2021
Available online 12 August 2021

overpotential is essential for the design and application of high-quality LIB.

In general, diffusion of Li-ions inside the positive and negative electrodes, diffusion and migration of ions in the electrolyte, charge-transfer reactions at the electrode/electrolyte interfaces, and the electronic conduction in the electrodes and current collectors are commonly considered as dominant factors causing overpotentials [3–10]. Among these, Li-ion diffusion inside the electrodes is frequently considered as the rate-determining step for LIB [4,7,11]. Besides these internal battery properties, some external factors, such as the applied current density [12,13], temperature [14], State-of-Charge (SoC) [15], and State-of-Health (SoH) [15–17] also affect the overpotential. The relation of the overpotential with all these highly coupled factors becomes extremely complicated. In order to study these relations in more detail, the use of electrochemical models is essential.

Physics-based electrochemical models are widely used to describe the electrochemical performances of LIB [5,18–30]. Models based on the Nernst–Planck equation have been applied in the analyses of overpotentials for liquid electrolytes [26] and all-solid-state batteries [27,29,30]. In the Nernst-Planck approach, overpotentials caused by diffusion and migration of species are denoted as diffusion and migration overpotential components, respectively, and the overpotential related to the charge-transfer reaction at the electrode/electrolyte interface is denoted as charge-transfer overpotential.

The so-called pseudo-two-dimensional (P2D) model, using a combination of the porous electrode theory and concentrated solution theory [31,32], provides a basic theoretical framework for the physical and electrochemical processes taking place inside LIB. The P2D model has been extensively used to study the different above-described overpotential components [5,18–22]. However, in the literature, there are various notations of overpotential components. For example, the electrolyte overpotential in Refs. [5,19,22] refers to the electrolyte potential drop across the separator. In contrast, the electrolyte overpotential in Refs. [18,20] refers to the electrolyte potential difference across the entire battery stack from current collector to current collector. Similarly, kinetic, ohmic, and Li diffusion in electrode overpotentials often have different definitions [5,18–20,22], leading to seemingly different results.

The reaction-rate distribution inside the porous electrode, an important factor influencing overpotential components and battery performance, is non-uniform in real applications [33–35] and simulations [36,37], and is determined by numerous battery parameters [36–38]. However, it is frequently considered to be uniformly distributed [18,20] or added into another term called matrix overpotential [5,19,22]. Both of these two approaches are not helpful for a complete understanding of the dynamic behaviors of overpotential components. Therefore, it is very important to harmonize the generally accepted definitions and the full reflection of the battery status during (dis) charging in terms of the overpotential analyses.

In the present work, a battery composed of a graphite-based porous electrode and a Li metal counter electrode is selected as research subject to reduce the complexity of a full cell with two porous electrodes. The overpotential of a graphite-based porous electrode/Li battery is mathematically derived using the P2D model. The total overpotential is split into four overpotential components. Those are separately simulated and analyzed, resulting in various qualitative and quantitative conclusions. The simulation results reveal the influences of the non-uniform reaction-rate distribution inside the porous electrode on each overpotential component, showing interesting dynamic changes during operations. The results in the present paper help to understand the overpotential in P2D-modeled Li-ion batteries and provide insights for further improvement and optimization.

2. Model development

Fig. 1a presents the layout of a graphite-based porous electrode/Li

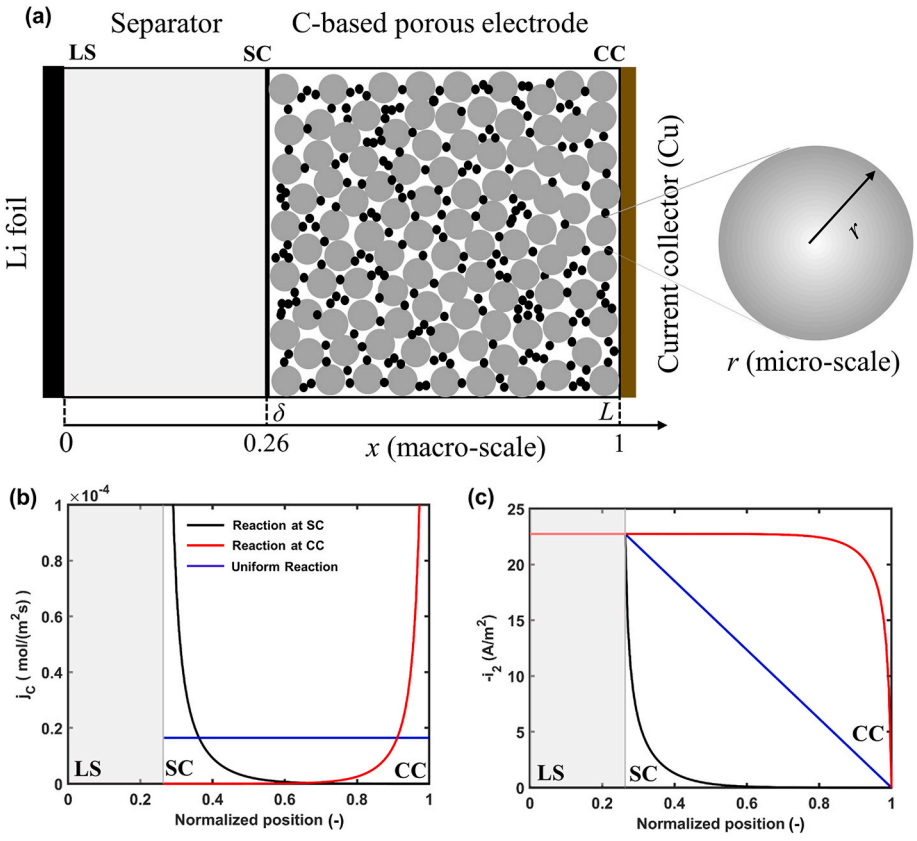

Fig. 1. (a) Layout of a P2D model for a C-based porous electrode/Li battery. The large gray solid circles denote active material particles, and the small black circles represent the conducting additives. (b) Reaction-rate distribution (j_C) inside the porous electrode, and (c) current-density distribution (i_2) in the electrolyte across the battery under three particular conditions at a 0.5 C-rate (I = −22.75 A/m^2). The black curves represent the condition of a dominant reaction-rate near the SC interface, the red lines represent a dominant reaction-rate near the CC interface, and the blue lines represent a uniformly distributed reaction-rate across the porous electrode. The gray areas indicate the separator region. Note that the ionic current density in the separator region is always equal to the total applied current density (I). (For interpretation of the references to color in this figure legend, the reader is referred to the Web version of this article.)

battery, including a metallic Li foil negative electrode, a porous separator membrane, and a porous graphite-based positive electrode soaked into the liquid electrolyte. δ denotes the thickness of the porous separator and L the distance between the Li metal electrode and the Cu current collector. The thickness of the graphite-based porous electrode is equal to $L-\delta$. The Li metal/separator (LS) interface is defined at the position $x=0$, the separator/graphite-based porous electrode (SC) interface at $x=\delta$, and the graphite-based electrode/Cu current collector (CC) interface at $x=L$. The numbers along the x-direction represent normalized positions of the interfaces, which are derived from the experimental data listed in Table 2. The electrochemical reactions taking place inside this battery during (dis)charging are represented as

$$C_6 + yLi^+ + ye^- \underset{\text{discharge}}{\overset{\text{charge}}{\rightleftharpoons}} Li_yC_6, \quad (1)$$

$$yLi \underset{\text{discharge}}{\overset{\text{charge}}{\rightleftharpoons}} yLi^+ + ye^- \ . \quad (2)$$

Eqs. (1) and (2) describe the reactions at the C_6 and Li electrodes, respectively. C_6 denotes the graphite-based porous electrode, further simplified as C. Charging the C-based electrode/Li cell implies delithiation of the C-based electrode, and discharging denotes the lithiation of the C-based electrode. Nowadays, a small amount of Si or SiO_x is frequently added to the graphite electrode to increase the storage capacity. The C-based electrode used in this work is blended with a small amount of Si. The applied model in this work assumes a C-based electrode in which the effect of Si is considered by using modified parameters that are reported in Section 4. A similar approach has also been used for modeling silicon-graphite-based batteries [39] and other batteries with blended active electrode materials [40–42].

The P2D model is adopted to describe the various physical and electrochemical processes occurring in the C-based electrode/Li cell. The governing equations are summarized in Table 1. These equations include the mass balance in the electrolyte (Eqs. T3 and T9), the electric potential distribution in the electrode (Eq. T11) and electrolyte (Eqs. T4 and T10), the charge balance (Eqs. T12 and T13), the charge-transfer kinetics (Eqs. T1-T2, and T6-T8), and the diffusion in the spherical electrode particles (Eq. T5). The battery output voltage is listed in Eq. T14. All parameter definitions are listed in the nomenclature.

The battery voltage (V_{bat}) is given by Eq. T14, which can be further expanded with the help of Eq. T7, leading to

Table 2
P2D model parameters, values, and units.

Symbol	Value	Unit
c_2^0	1000[a]	mol m^{-3}
D_2	$6.2{\cdot}10^{-10}$[b]	m^2 s^{-1}
D_1	$2.4{\cdot}10^{-14}$[b]	m^2 s^{-1}
k_C	$4.0{\cdot}10^{-11}$[b]	m$^{2.5}$ mol$^{-0.5}$ s^{-1}
R_1	$11{\cdot}10^{-6}$[a]	m
R_f	5[b]	Ωcm^2
t_+	0.363[d]	–
T	298[c]	K
α, α_{Li}	0.5, 0.5[b]	–
δ	$25{\cdot}10^{-6}$[a]	m
L	$95{\cdot}10^{-6}$[c]	m
ε_m	0.39[a]	–
ε_C	0.25[a]	–
ε_f	0.02[b]	–
$brugg_m$	2.2[b]	–
$brugg_C$	2.95[b]	–
κ	$1.58{\cdot}10^{-3}c_2\exp[-0.85(c_2{\cdot}10^{-3})^{1.4}]$[d]	S m^{-1}
σ	1000[a]	S m^{-1}
a	$3(1-\varepsilon_C-\varepsilon_f)/R_1$	m^{-1}

[a] Provided by the manufacturer.
[b] Estimated values from the model.
[c] Measured.
[d] Taken from Ref [11].

Table 1
Governing equations in the P2D model for a C-based porous electrode/Li battery.

Region		Governing equations	Eq. nr.	Boundary and initial conditions
Li foil $x=0$	Kinetics	$I = i_{Li}^0\left[\exp\left(\frac{\alpha_{Li}F\eta_{Li}^{ct}}{RT}\right) - \exp\left(-\frac{(1-\alpha_{Li})F\eta_{Li}^{ct}}{RT}\right)\right]$	T1	–
		$i_{Li}^0 = Fk_{Li}c_2^{\alpha_{Li}}$	T2	–
Separator membrane $0<x\le\delta$	Mass balance	$\varepsilon_m\frac{\partial c_2}{\partial t} = \frac{\partial}{\partial x}\left[D_2^m\frac{\partial c_2}{\partial x}\right]$	T3	$-D_2^m\frac{\partial c_2}{\partial x}\Big\vert_{x=0} = \frac{I(1-t_+)}{F}, \quad D_2^m\frac{\partial c_2}{\partial x}\Big\vert_{x=\delta} = D_2^C\frac{\partial c_2}{\partial x}\Big\vert_{x=\delta}$
	Potential in solution	$i_2 = -\kappa_m\frac{\partial\Phi_2}{\partial x} + \frac{2\kappa_m RT}{F}(1-t_+)\frac{\partial \ln c_2}{\partial x}$	T4	$i_2 = I$
C-based electrode $\delta\le x\le L$	Diffusion in the particle	$\frac{\partial c_1}{\partial t} = \frac{1}{r^2}\frac{\partial}{\partial r}\left(r^2D_1\frac{\partial c_1}{\partial r}\right)$	T5	$-D_1\frac{\partial c_1}{\partial r}\Big\vert_{r=R_1} = j_C, \ \frac{\partial c_1}{\partial r}\Big\vert_{r=0} = 0$ $c_1(r,0)\vert_{t=0} = c_1^0$
	Kinetics	$j_C = \frac{i_C^0}{F}\left[\exp\left(\frac{\alpha F\eta_C^{ct}}{RT}\right) - \exp\left(-\frac{(1-\alpha)F\eta_C^{ct}}{RT}\right)\right]$	T6	–
		$\eta_C^{ct} = \Phi_1 - \Phi_2 - U_C(c_1^s, T)$	T7	–
		$i_C^0 = Fk_C(c_1^{max}-c_1^s)^\alpha(c_1^s)^{1-\alpha}(c_2)^\alpha$	T8	–
	Mass balance	$\varepsilon_C\frac{\partial c_2}{\partial t} = \frac{\partial}{\partial x}\left[D_2^C\frac{\partial c_2}{\partial x}\right] + aj_C(1-t_+)$	T9	$D_2^m\frac{\partial c_2}{\partial x}\Big\vert_{x=\delta} = D_2^C\frac{\partial c_2}{\partial x}\Big\vert_{x=\delta}, \quad D_2^C\frac{\partial c_2}{\partial x}\Big\vert_{x=L} = 0$
	Potential in solution	$i_2 = -\kappa_C\frac{\partial\Phi_2}{\partial x} + \frac{2\kappa_C RT}{F}(1-t_+)\frac{\partial \ln c_2}{\partial x}$	T10	$i_2\vert_{x=\delta} = I, i_2\vert_{x=L} = 0$
	Potential in solid	$i_1 = -\sigma_C\frac{\partial\Phi_1}{\partial x}$	T11	$i_1\vert_{x=\delta} = 0, i_1\vert_{x=L} = I$
		$i_1 + i_2 = I$	T12	–
		$aj_C = \frac{1}{F}\frac{\partial i_2}{\partial x}$	T13	–
Battery	Output voltage	$V_{bat} = \Phi_1\vert_{x=L} - \Phi_1\vert_{x=0} - R_fI$	T14	–

$$\begin{aligned} V_{bat} &= \Phi_1|_{x=L} - \Phi_1|_{x=0} - R_f I \\ &= \left(\eta_C^{ct} + U_C(c_1^s) + \Phi_2\right)|_{x=L} - \left(\eta_{Li}^{ct} + U_{Li} + \Phi_2\right)|_{x=0} - R_f I \\ &= \left(\Phi_2|_{x=L} - \Phi_2|_{x=0}\right) + \left(U_C(c_1^s)|_{x=L} - U_{Li}|_{x=0}\right) + \eta_C^{ct}|_{x=L} - \eta_{Li}^{ct} - R_f I \\ &= \left(\Phi_2|_{x=L} - \Phi_2|_{x=0}\right) + U_C(c_1^s)|_{x=L} + \left(\eta_C^{ct}|_{x=L} - \eta_{Li}^{ct}\right) - R_f I, \end{aligned} \tag{3}$$

where $\Phi_1|_{x=L}$ and $\Phi_1|_{x=0}$ are the electrostatic potentials at the CC and the LS interfaces, respectively. R_f is the summation of the ohmic resistance of the current collectors and contact resistances between the current collectors and electrodes, U_C is the equilibrium potential of the C-based electrode, Φ_2 is the potential in the electrolyte, and U_{Li} is the equilibrium potential of the Li metal electrode, by definition equal to zero. η_C^{ct} and η_{Li}^{ct} are the charge-transfer overpotentials at the C-based electrode and metallic Li electrode, respectively. V_{bat} is the output voltage of the battery under non-equilibrium conditions, and I is the applied current density.

The total overpotential (η_{bat}) is considered as the difference between the battery output voltage (V_{bat}) under non-equilibrium conditions and the equilibrium potential (U_{bat}), with $U_{bat} = U_C - U_{Li} = U_C$ in the present, specific, case with $U_{Li} = 0$. η_{bat} can then be written as

$$\begin{aligned} &\eta_{bat} = V_{bat} - U_{bat} = \left(\Phi_2|_{x=L} - \Phi_2|_{x=0}\right) + \\ &\left(U_C(c_1^s)|_{x=L} - U_C\left(\bar{c}_1\right)\right) + \left(\eta_C^{ct}|_{x=L} - \eta_{Li}^{ct}|_{x=0}\right) - R_f I\,. \end{aligned} \tag{4}$$

η_{bat} is now composed of four terms:

(i) The electrolyte potential difference between the CC and LS interfaces ($\Phi_2|_{x=L} - \Phi_2|_{x=0}$), further denoted as the electrolyte overpotential (η_2),
(ii) the potential difference between the electrode potential at the CC interface and the equilibrium potential of the C-based electrode caused by non-uniform Li concentrations in the electrode ($U_C(c_1^s)|_{x=L} - U_C(\bar{c}_1)$), further denoted as Li concentration overpotential in the electrode (η_1^c),
(iii) the kinetic overpotential related to the charge-transfer reactions at the CC and LS interfaces ($\eta_C^{ct}|_{x=L} - \eta_{Li}^{ct}|_{x=0}$), further denoted as kinetic overpotential (η^{ct}), and
(iv) the pure electrode ohmic contributions ($-R_f I$), further denoted as η_1^{Ω}.

These four terms and the total overpotential will be explained in detail in Sections 2.1-2.5.

2.1. Electrolyte overpotential

Eqs. T4 and T10 describe the electrolyte potential in the separator and the porous electrode region. Performing integration along with the x-coordinate leads to the following expressions

$$\begin{aligned} &\Phi_2(x,t) - \Phi_2(0,t) = -I\int_0^x \frac{dy}{\kappa_m(y,t)} + \\ &\frac{2RT}{F}\int_0^x (1 - t_+(y,t))d\ln c_2(y,t),\ 0 < x \le \delta, \end{aligned} \tag{5.1}$$

$$\begin{aligned} &\Phi_2(x,t) - \Phi_2(0,t) = -I\int_0^\delta \frac{dy}{\kappa_m(y,t)} - \int_\delta^x \frac{i_2(y,t)dy}{\kappa_C(y,t)} + \\ &\frac{2RT}{F}\int_0^x (1 - t_+(y,t))d\ln c_2(y,t),\ \delta < x \le L, \end{aligned} \tag{5.2}$$

where κ_m and κ_C represent the effective ionic conductivity in the separator and C-based porous electrode region, respectively. The potential difference in the electrolyte between the CC and LS interfaces, denoted as the *electrolyte overpotential* (η_2), can therefore be written as

$$\begin{aligned} \eta_2 &= \Phi_2|_{x=L} - \Phi_2|_{x=0} = \Phi_2(L,t) - \Phi_2(0,t) \\ &= -I\int_0^\delta \frac{dy}{\kappa_m(y,t)} - \int_\delta^L \frac{i_2(y,t)dy}{\kappa_C(y,t)} + \\ &\frac{2RT}{F}\int_0^L (1 - t_+(y,t))d\ln c_2(y,t), \end{aligned} \tag{6}$$

which can be split into two parts. The first two terms after the third equal sign of Eq. (6) can be defined as the *electrolyte ohmic overpotential* (η_2^{Ω}) and the third term considers the *electrolyte concentration overpotential* (η_2^c). Eq. (6) can then be rewritten as

$$\eta_2 = \Phi_2|_{x=L} - \Phi_2|_{x=0} = \eta_2^c + \eta_2^{\Omega}\ , \tag{7.1}$$

$$\eta_2^c = \frac{2RT}{F}\int_0^L (1 - t_+(y,t))d\ln c_2(y,t)\ , \tag{7.2}$$

$$\eta_2^{\Omega} = -I\int_0^\delta \frac{dy}{\kappa_m(y,t)} - \int_\delta^L \frac{i_2(y,t)dy}{\kappa_C(y,t)}\ , \tag{7.3}$$

where η_2^c is a function of the transference number of Li-ions (t_+) and electrolyte concentration gradients across the battery, assuming that the temperature (T) and thickness (L) are constant. η_2^{Ω} is a function of the applied current density (I), the current density distribution in the electrolyte (i_2), the porosity of the porous electrode and separator (ε_m, ε_C), and the effective ionic conductivities (κ_m and κ_C), assuming that thicknesses of the separator and porous electrode (δ, $L - \delta$) are constant.

During short-time or low-current applications, when hardly any electrolyte concentration gradients can be built up, κ_m, κ_C and t_+ are constant. Eqs. (7.2) and (7.3) can then be further simplified to

$$\eta_2^c = \frac{2RT}{F}(1 - t_+)\ln\frac{c_2(L,t)}{c_2(0,t)} \tag{8.1}$$

$$\eta_2^{\Omega} = -\frac{I\delta}{\kappa_m} - \frac{1}{\kappa_C}\int_\delta^L i_2(y,t)dy \tag{8.2}$$

respectively. From Eq. (8.2), it follows that the ionic current density in the electrolyte (i_2) is a key variable for the calculation of η_2^{Ω}. From the charge conservation in Eq. T12 and boundary conditions T4, T10, and T11, it follows that i_2 in the separator region always equals I and decreases from I at the SC interface to 0 at the CC interface.

In the porous electrode region, two boundary cases and one average case of the distribution of i_2 can be considered, leading to minimum, maximum, and average values for η_2^{Ω}. These particular cases are numerically calculated and shown in Fig. 1b and c. Fig. 1b shows the reaction-rate distribution (j_C), and Fig. 1c shows the ionic current density in the electrolyte (i_2) at a 0.5 C-rate (1C = 45.5 A/m^2). The black curves represent a situation when the reaction-rate is dominant near the SC interface, leading to a minimum value of η_2^{Ω}. The red lines represent a dominant reaction near the CC interface, leading to a maximum value of η_2^{Ω}, and the blue lines represent a uniformly distributed reaction rate across the porous electrode, leading to an average value of η_2^{Ω}. Eqs. (S1-S6) in the Supporting Information give the derivations of η_2^{Ω} for these three particular cases.

2.2. Li concentration overpotential in the electrode

The second term in Eq. (4) represents the potential difference between the particle surface potential at the CC interface and the equilibrium potential. It is called the *Li concentration overpotential in the electrode* (η_1^c), which is defined as

$$\eta_1^c = U_C(c_1^s)|_{x=L} - U_C(\bar{c}_1)\ . \tag{9}$$

The particle surface potential in the electrode is expressed as a

function of the Li concentration at the particle surface (c_1^s), which changes along the x-direction of the porous electrode. The equilibrium potential is a function of the average Li concentration ($\bar{c}_1$) in the electrode under equilibrium conditions. To further derive Eq. (9) into separate overpotential components, a so-called local average Li concentration c_1^{la} in each particle needs to be defined, namely $c_1^{la} = c_1^{la}(x,t) = \frac{3}{R_1^3}\int_0^{R_1} c_1(x,r,t)r^2dr$. $\bar{c}_1$ and c_1^{la} are, in general, not equal to each other, because $\bar{c}_1 = \bar{c}_1(t) = \frac{1}{(L-\delta)}\int_\delta^L c_1^{la}(x,t)dx$. With these notations, Eq. (9) can be expanded to

$$\begin{aligned}\eta_1^c &= U_C(c_1^s)|_{x=L} - U_C(\bar{c}_1)\\ &= U_C(c_1^s)|_{x=L} - U_C(c_1^{la})|_{x=L} + \\ &U_C(c_1^{la})|_{x=L} - U_C(\bar{c}_1)\\ &= \eta_1^d + \eta_1^r\ ,\end{aligned} \tag{10.1}$$

in which η_1^d and η_1^r are defined as

$$\eta_1^d = U_C(c_1^s)|_{x=L} - U_C(c_1^{la})|_{x=L} \tag{10.2}$$

and

$$\eta_1^r = U_C(c_1^{la})|_{x=L} - U_C(\bar{c}_1)\ , \tag{10.3}$$

respectively. In Eq. (10.2), η_1^d represents the Li concentration diffusion overpotential in the electrode particles at the CC interface, which is generated by the concentration gradient in the radial direction of these particles. In Eq. (10.3), η_1^r denotes the Li concentration overpotential among all solid particles. η_1^r is formed by the Li concentration gradient across particles, which is a result of the non-uniform reaction-rate distribution. The explained two concentration gradients together form the Li concentration overpotential in the electrode (η_1^c). When the current is switched off η_1^d, and η_1^r will drive the concentrations within each particle and across all particles equal, *i.e.* $c_1^s = c_1^{la} = \bar{c}_1$. The movement of Li-ions across different particles is caused by the overpotential, which leads to electrochemical reactions at the electrode particle interfaces [43]. Note that the total net influx of Li ions for all solid particles is equal to zero during a zero-current period.

2.3. Kinetic overpotential

The third term in Eq. (4) expresses the charge-transfer overpotential difference between the LS and CC interfaces, denoted as the *kinetic overpotential* (η^{ct}). For both the C-based porous electrode and Li metal electrode, the Butler-Volmer equations apply and can be written as

$$j_C = \frac{i_C^0}{F}\left[\exp\left(\frac{\alpha F\eta_C^{ct}}{RT}\right) - \exp\left(-\frac{(1-\alpha)F\eta_C^{ct}}{RT}\right)\right] \tag{11.1}$$

$$I = i_{Li}^0\left[\exp\left(\frac{\alpha_{Li}F\eta_{Li}^{ct}}{RT}\right) - \exp\left(-\frac{(1-\alpha_{Li})F\eta_{Li}^{ct}}{RT}\right)\right] \tag{11.2}$$

accordingly. Eq. (11.1) applies to each particle surface across the porous C-based electrode, and Eq. (11.2) only holds at the metallic Li surface.

For convenience, we now define a function $G_{y,z}(\eta) = \exp(yz\eta) - \exp(-(1-y)z\eta)$, where $y = \alpha$ and $z = F/RT$. Eqs. (11.1) and (11.2) can then be represented by

$$j_C = \frac{i_C^0}{F}G_{\alpha,F/(RT)}(\eta_C^{ct}) \tag{12.1}$$

$$I = i_{Li}^0 G_{\alpha_{Li},F/(RT)}(\eta_{Li}^{ct}) \tag{12.2}$$

respectively. With these notations, the charge-transfer overpotentials of the C-based and Li metal electrode can now be expressed as

$$\eta_C^{ct} = G_{\alpha,F/(RT)}^{-1}\left(\frac{j_C F}{i_C^0}\right) \tag{13.1}$$

$$\eta_{Li}^{ct} = G_{\alpha_{Li},F/(RT)}^{-1}\left(\frac{I}{i_{Li}^0}\right) \tag{13.2}$$

where $G_{y,z}^{-1}$ is a function inverse to $G_{y,z}$. In these notations, the kinetic overpotential term in Eq. (4) can be expanded as

$$\begin{aligned}\eta^{ct} &= \eta_C^{ct}|_{x=L} - \eta_{Li}^{ct}|_{x=0}\\ &= G_{\alpha,F/(RT)}^{-1}\left(\frac{Fj_C}{i_C^0}|_{x=L}\right) - G_{\alpha_{Li},F/(RT)}^{-1}\left(\frac{I}{i_{Li}^0}\right)\end{aligned} \tag{14}$$

Eq. (14) includes the charge-transfer overpotentials at the CC and LS interfaces.

2.4. Electrode ohmic overpotential

The last term in Eq. (4) is the *electrode ohmic overpotential* ($\eta_1^\Omega = -R_f I$), resulting from the ohmic resistance from the electrode and current collectors, including the SEI film resistance and the connection issues between current collectors, metal leads, and other electronic components. This electrode ohmic overpotential is considered a minor contribution and adopted as an empirical constant in the present paper.

2.5. Total overpotential

Combining the results from the previous sections, the total overpotential of the C-based porous electrode/Li battery can be described by

$$\eta_{bat} = V_{bat} - U_{bat} = \eta_2 + \eta_1^c + \eta^{ct} + \eta_1^\Omega = \eta_1^c + \eta_2^c + \eta^{ct} + \eta_1^\Omega + \eta_2^\Omega\ . \tag{15.1}$$

Finally, the following concise set of equations can be used for calculating the four overpotentials

$$\begin{aligned}\eta_1^c &= \eta_1^d + \eta_1^r = \left(U_C(c_1^s)|_{x=L} - U_C(c_1^{la})|_{x=L}\right)\\ &+\left(U_C(c_1^{la})|_{x=L} - U_C(\bar{c}_1)\right)\ ,\end{aligned} \tag{15.2}$$

$$\eta_2^c = \frac{2RT}{F}\int_0^L (1-t_+)d\ln c_2\ , \tag{15.3}$$

$$\eta^{ct} = G_{\alpha,F/(RT)}^{-1}\left(\frac{Fj_C}{i_C^0}|_{x=L}\right) - G_{\alpha_{Li},F/(RT)}^{-1}\left(\frac{I}{i_{Li}^0}\right)\ , \tag{15.4}$$

$$\eta_1^\Omega = -R_f I, \tag{15.5}$$

$$\eta_2^\Omega = -\left(I\int_0^\delta \frac{dy}{\kappa_m} + \int_\delta^L \frac{i_2 dy}{\kappa_C}\right) \tag{15.6}$$

3. Experimental

Fresh commercial 18650-type cylindrical batteries manufactured by Tianjin Lishen Battery Co., Ltd were dismantled in an argon-filled glove box, and pieces of C-based anodes were taken out. Prior to the measurements, the active material on one side of the double-coated C-based electrode was carefully scraped off with a sharp blade and cut into discs with a diameter of 14 mm (the active material mass is around 17.5 mg). 2032-type coin cells were subsequently assembled using the as-prepared C-based electrodes as the working electrodes and Li metal foil as the counter electrodes. A 2400-type Celgard separator (thickness 25 μm) and 1 M $LiPF_6$ electrolyte in the solvent mixture of EC:DMC:DEC with a 1:1:1 volume ratio were used.

The electrochemical properties of the assembled cells were measured by a Neware battery cycler in the voltage range of 0.01–2 V at 25 °C. Before the test, the cells were equilibrated for 12 h and then activated for

four cycles with a 0.2 C-rate current (1C = 7 mA or 45.5 A/m^2) in the constant-current charging mode (delithiation of C-based electrode) and the constant-current constant-voltage (CCCV) discharging mode (lithiation of C-based electrode). The cut-off current in CCCV mode was set at 0.04C. Then, characterization cycles were performed, in which a 0.2 C-rate discharge current was used in the CCCV mode, and a set of constant charging currents (0.04, 0.1, 0.2, 0.5, 1.0, and 1.4C) was applied in sequence. The rest period between charging and discharging was set to 30 min. The pseudo open-circuit voltage (OCV) was obtained at a 0.01 C-rate current under 25 °C.

Simulations were performed in the software Matlab R2018b. The finite volume method was used to discretize the partial differential equations (PDE) listed in Table 1. The forward Euler method was adopted to solve these equations. The parameter values are listed in Table 2. The temperature in the simulation was set to 25 °C, which is the same as that in the experiments.

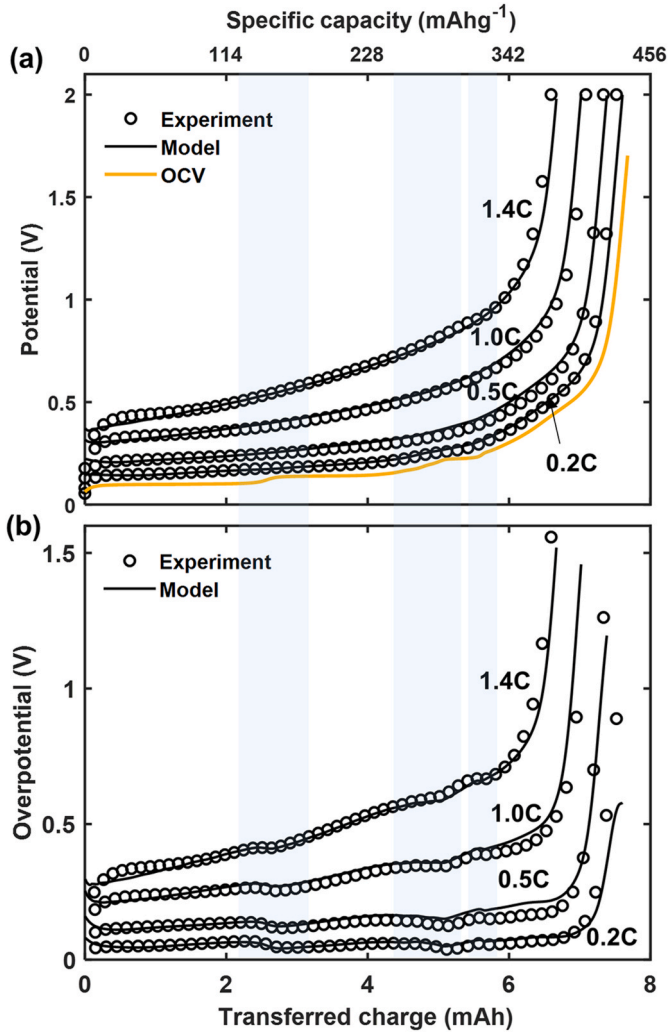

Fig. 2. (a) Comparison of the experimental (symbols) and simulated (black lines) voltage charging curves at various C-rates. The golden line represents the OCV of a C-based electrode/Li cell. (b) Comparison of experimental (symbols) and simulated (lines) overpotentials at various C-rates. The x-axis at the bottom gives the transferred charge in mAh, and the x-axis at the top gives the corresponding specific capacity in mAhg-1. The active electrode material is graphite blended with a small amount of Si. The theoretic capacity is in the range from 477.51 to 554.90 mAhg^{-1}, considering the atomic ratio of Si/C of 1.41–2.35 %, which is obtained from multiple Scanning Electron Microscope (SEM) tests equipped with Energy-dispersive X-ray Spectroscopy (EDX). (For interpretation of the references to color in this figure legend, the reader is referred to the Web version of this article.)

4. Results and discussion

Fig. 2a compares the experimental and the simulated voltage curves of the C-based electrode/Li battery with the optimized parameter set in Table 2 using 0.2, 0.5, 1.0, and 1.4 C-rate charging currents. Fig. 2b shows the experimental and simulated overpotentials. Note that charging the C-based electrode/Li cell implies delithiation of the C-based electrode. The black circles and lines represent the experimental and simulated results, respectively. Good agreement is found between the simulations and experiments for the voltages (Fig. 2a) and overpotentials (Fig. 2b) at all C-rates. The gold-colored curve in Fig. 2a shows the OCV of the battery. The OCV of the battery shows several plateaus and slope regions, which are related to the two-phase and one-phase during Li-intercalation in the graphite electrode [44,45]. These features become less visible when a current is applied, especially at C-rates $\geq$0.2. Due to a lack of space between the 0.2C voltage curve and OCV curve in Fig. 2a, the experimental and simulated results for 0.04 and 0.1C are presented individually in Fig. S1, in which these plateau- and slope-features still can be observed. Other researchers have also found the disappearance of the plateau and slope features in the voltage (dis)charge for C-based electrodes [46,47] at higher C-rates. Switching off the current periodically followed by relaxations at moderate (or high) C-rates makes the stages appear again at the end of relaxations, as indicated by the open-circle dash lines of GITT measurement in Fig. S2, where the currents of 0.1, 0.2 and 0.5C are used during the current pulses. Intuitively, the overpotentials should be responsible for these observations. It can be seen that evident variations and dynamic changes are found near the sloping regions of the OCV, as indicated by the shaded areas in Fig. 2. To investigate these intrinsic phenomena, an analysis of the various overpotential components is presented in Sections 4.1-4.5 with the model described in Section 2 and the optimized parameter set listed in Table 2.

To understand the dynamic behavior of the various overpotential components, presented in Sections 4.1-4.5, the (normalized) reaction-rate distribution is introduced. The reaction-rate distribution (j_C) inside the porous electrode, as represented by Eq. T6, is a common and recurring state in this work and leads to coupled relations among the various overpotential components. At short-time scales j_C is determined by a few key battery parameters, such as effective ionic and electronic conductivity, applied current density, and exchange current density [37,38], and can be derived analytically. At long-time scales, j_C is an implicit function of the parameters indicated for the short-time scale, and all fluxes and concentrations in the system and therefore can only be obtained numerically.

Fig. 3 shows the numerically calculated normalized reaction-rate distribution (j_C/j_C^u) as a function of normalized position and transferred charge to at (a) 1.4, (b) 1.0, (c) 0.5, and (d) 0.2 C-rate. The normalized reaction-rate distribution is obtained through dividing j_C by the uniform reaction-rate distribution (j_C^u), a constant at each C-rate, which is calculated according to

$$j_C^u = -\frac{I}{a(L-\delta)F} \tag{16}$$

When adopting j_C^u for a porous electrode model, the model becomes a so-called average model (AM) [18,48]. Fig. S3 shows j_C^u at various C-rates as a function of normalized position and charge. It can be seen that j_C^u obviously is constant at each C-rate, but the level is strongly dependent on the C-rate.

In Fig. 3, each figure is a combination of a surface plot and a semi-transparent pink plane. The surface plot represents j_C/j_C^u, and the pink plane represents the constant reaction-rate distribution $j_C/j_C^u = 1$. It should be noted that j_C behaves exactly the same as j_C/j_C^u because j_C^u is a constant at each C-rate. Using j_C/j_C^u will give a direct comparison of (non)uniformity of j_C at various C-rate. When j_C is more non-uniform, j_C/j_C^u deviates much from the pink planes. Contrastingly, when j_C

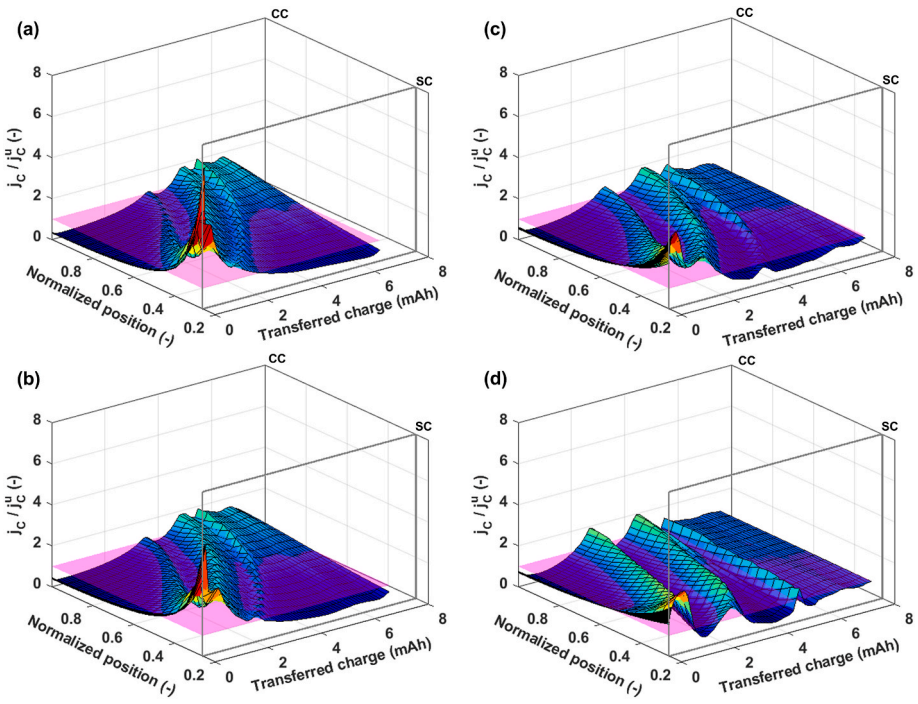

Fig. 3. Normalized reaction-rate distributions (j_C/j_C^u) as a function of normalized position and transferred charge at (a) 1.4, (b) 1, (c) 0.5, and (d) 0.2 charging C-rate. j_C represents a non-uniform reaction-rate distribution from the model and j_C^u represents a uniform reaction-rate distribution as shown in Eq. (16). The rectangular frames at the normalized position of 0.26 and 1 represent the SC and CC interfaces.

approaches uniformity, j_C/j_C^u converges to the indicated planes. It can be seen that j_C is non-uniform for all C-rates, and that non-uniformity increases at higher C-rates. For each C-rate, the largest deviations take place at the SC interface at 0–2 mAh of the transferred charge, while only minor reactions happen inside the electrode at this charge range. After 2 mAh, j_C/j_C^u is fluctuating around the pink planes, indicating the reactions are relatively uniform compared to the range of 0–2 mAh.

In addition, various waves can be observed in j_C/j_C^u at all C-rates in Fig. 3. The waves propagate from the SC to the CC interface as a function of transferred charge and position inside the porous electrode. From literature [32,43] and simulations presented here, it can be concluded that the wave of j_C/j_C^u is caused by the sloping (solid-solution) regions in

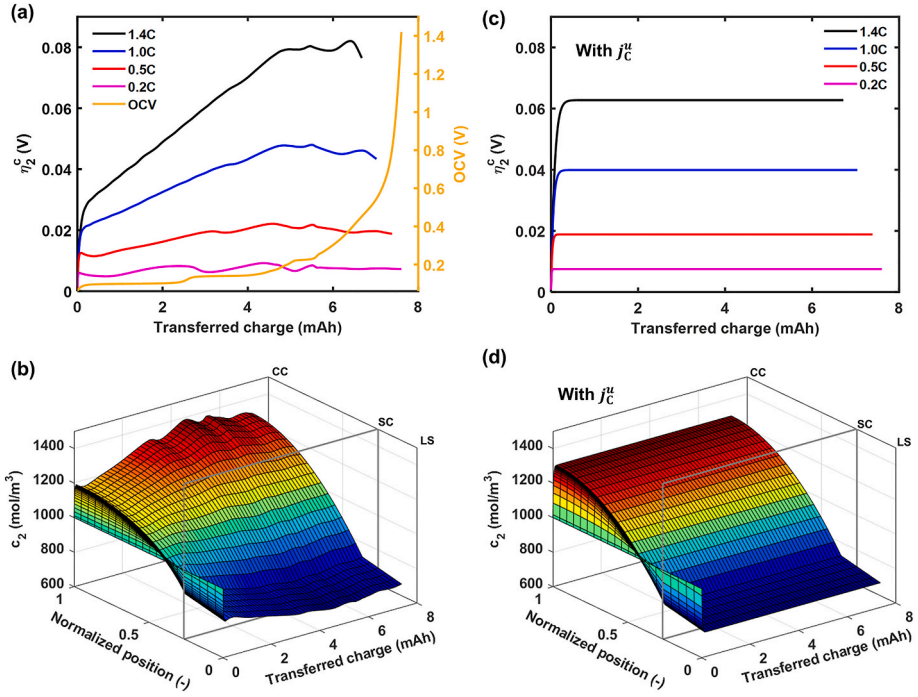

Fig. 4. (a) Comparison of electrolyte concentration overpotential (η_2^c) at various C-rates with the OCV as a reference. (b) The c_2 profile as a function of normalized position and transferred charge under a 0.5C charging current. (c) η_2^c at various C-rates with assumptions of j_C^u. (d) c_2 profile at 0.5C with j_C^u. The normalized position at 0, 0.26, and 1 represents the LS, SC, and CC interface.

the OCV curve, and the number of waves is therefore equal to the number of the sloping regions in the OCV curve. For example, the first wave in Fig. 3a–d corresponds to the first sloping region in the OCV curve at a transferred charge of around 2.5 mAh (golden curve in Fig. 2a). It is worth mentioning that the battery OCV determines the evolution of the waves in j_C/j_C^u (or j_C) through dictating the particle surface potential ($U_C(c_1^s)$) [49]. Fig. S4 presents $U_C(c_1^s)$ for each particle as a function of transferred charge at various C-rates. During the operations, $U_C(c_1^s)$ is changing with the position inside the porous electrode and transferred charge. The sloping regions in $U_C(c_1^s)$ for each particle (Fig. S4) cause the disturbances in the local charge-transfer overpotential, finally resulting in the wave formation and evolution in j_C [49]. Moreover, the variation of $U_C(c_1^s)$ among all particles (*e.g.* horizontal direction of various lines in Fig. S4) is small at low C-rates but large at high C-rates (Fig. S4), explaining why the waves in j_C/j_C^u (or j_C) cross over wide ranges in the transferred charge at high C-rates.

Now a good overview of j_C inside the porous electrode is given, and the analysis of each overpotential components will be described in detail below.

4.1. Electrolyte concentration overpotential

Using the mathematical analysis in Sections 2.1 and 2.5, the electrolyte concentration overpotential (η_2^c) can be analyzed and explained. According to Eqs. (15.3) and (7.2), η_2^c depends on c_2, t_+, T, and the battery geometric parameters. Fig. 4a presents the simulated η_2^c as a function of the transferred charge at different charging rates. The OCV (gold-colored line) is shown again as reference curve. It can be seen that η_2^c increases with increasing C-rates and shows clear fluctuations at all C-rates. These fluctuations become more pronounced near the sloping regions in the OCV curve, *i.e.* at 2–3 and 4–6 mAh of transferred charge.

According to Eq. (15.3), η_2^c is only related to c_2 as the other parameters are constant. To explain the fluctuations in η_2^c, Fig. 4b shows the profile of c_2 in the battery as a function of transferred charge and normalized position upon charging with 0.5C. Fluctuations in c_2 can be observed with increasing charge, especially near the current collector. As described by the governing equations of the mass balance in the electrolyte (Eq. T9 for the porous electrode and Eq. T3 for the separator region), c_2 depends only on the mass transport in the separator region, while both the mass transport and j_C influence c_2 in the porous electrode region. In the simulations, the mass transport parameters (t_+ and D_2) are set constant (Table 2). Therefore, j_C is responsible for the fluctuations in c_2, which further determines the changes in η_2^c. The corresponding j_C profiles in Fig. 3c at 0.5C show multiple waves, clearly corresponding to the fluctuations in η_2^c and c_2 in Fig. 4a and b, respectively.

To prove the explanation above, simulations have been performed with the assumption of a constant j_C^u, as indicated by Eq. (16) and Fig. S3. Fig. 4c shows the simulation results of η_2^c for all C-rates and Fig. 4d shows the corresponding c_2 profile at 0.5 C-rate under the same assumption. Comparing Fig. 4b with d shows that c_2 in Fig. 4d does not reveal any fluctuations after a very short transient state, also leading to flat η_2^c curves in Fig. 4c without any fluctuations. This clearly indicates that the fluctuations in η_2^c are caused by changes in c_2, which in turn is caused by the dynamic behavior of j_C in Fig. 3. The increase of η_2^c as a function of C-rate in Fig. 4a is therefore the result of increasing gradients in c_2 at higher currents.

4.2. Li concentration overpotential in the electrode

η_1^c, the concentration overpotential in the electrode (Eq. (15.2)), results from the Li concentration gradient in the electrode particles, as mathematically explained in Section 2.2. Fig. 5a shows η_1^c at various charging C-rates together with the OCV curve as a reference, the inset shows corresponding enlargements. Apparently, η_1^c reveals only very small values at the beginning of charging but becomes very large at the end. In addition, two interesting features can be observed: *(i)* negative values for η_1^c at about 3 and 5 mAh, and *(ii)* these values become wider and more negative with increasing C-rates.

To explain the features observed in Fig. 5a, the two components contributing to η_1^c (Eq. (10.1)), η_1^d and η_1^r, are separately shown in Fig. 5b

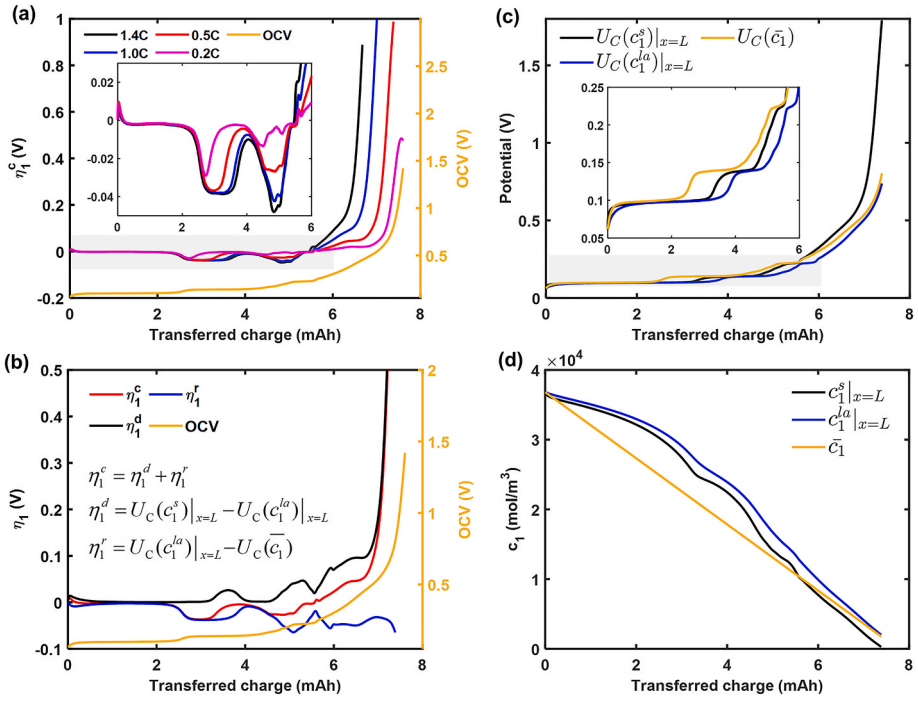

Fig. 5. (a) Comparison of the Li concentration overpotential (η_1^c) in the electrode at various charging C-rates and the OCV curve as a reference, (b) the separation of η_1^c into η_1^d and η_1^r at 0.5 C-rate, (c) $U_C(c_1^s)|_{x=L}$, $U_C(c_1^{la})|_{x=L}$ and $U_C(\bar{c}_1)$ voltage curves at 0.5 C-rate, and (d) various particle-related concentrations as a function of transferred charge. The insets in (a) and (c) are magnifications of the indicated shaded regions.

for a charging current of 0.5C. As defined in Section 2.2, η_1^d represents the Li diffusion overpotential within the particles at the CC interface (Eq. (10.2)), which is the result of the Li concentration gradient in the radial direction of the particles at the CC interface. η_1^r denotes the Li concentration overpotential across solid particles (Eq. (10.3)), which is a result of the Li concentration gradient across all solid particles induced by the non-uniform j_C. It can be seen in Fig. 5b that η_1^d (black line) always shows positive values and is responsible for the high values of η_1^c (red line) at the end of charging. η_1^r (blue line in Fig. 5b) always shows negative values and is therefore (most) responsible for the negative valleys in η_1^c. At the negative valleys of η_1^c, η_1^d also shows right-shifted positive peaks with respect to the sloping regions in the OCV.

Since the equations of η_1^d and η_1^r are composed of $U_C(c_1^s)|_{x=L}$, $U_C(c_1^{la})|_{x=L}$ and $U_C(\bar{c}_1)$, these three terms are shown separately in Fig. 5c for charging at 0.5C to explain the features observed in Fig. 5a and b. Note that all these three potentials are a function of the Li concentration in the solid. For this reason, c_1^s and c_1^{la} for the particles at the CC interface, and $\bar{c}_1$ are shown in Fig. 5d as a function of transferred charge. During charging (delithiation of the graphite-based electrode), c_1^s must be smaller than c_1^{la} because lithium is withdrawn from the particles surface (compare black and blue curves in Fig. 5d). Consequently, the potential $U_C(c_1^s)a|_{x=L}$ is higher than or nearly equal to $U_C(c_1^{la})|_{x=L}$ in Fig. 5c, leading to a non-negative η_1^d as shown in Fig. 5b. Between the sloping regions of $U_C(c_1^s)|_{x=L}$ and $U_C(c_1^{la})|_{x=L}$, η_1^d ($U_C(c_1^s)|_{x=L} - U_C(c_1^{la})|_{x=L}$) shows right-shifted positive peaks with respect to the sloping regions in the OCV curve ($U_C(\bar{c}_1)$ in Fig. 5c).

It should be noted that the Li concentrations in the particles are the cumulative results of j_C values through the whole previous period since the beginning of battery operation. That means j_C must be integrated over time to obtain the amount of Li extracted from a particle at a particular position in the electrode (see Fig. S5 for the cumulative calculation of Fig. 3c). As mentioned in literature [38,43,50–53] and shown in Fig. 3c and Fig. S5, considerably more reaction is taking place near the SC interface at the beginning of the charging, implying that $c_1^{la}|_{x=L}$ is larger than $\bar{c}_1$ as shown by blue and gold curves in Fig. 5d. It is interesting to observe the same behavior until the end of the process, as the blue curve is always higher than the gold line. This difference makes $U_C(c_1^{la})|_{x=L}$ smaller than or nearly equal to $U_C(\bar{c}_1)$ in Fig. 5c, causing η_1^r approaching zero or becoming negative, as found in Fig. 5b. Between the sloping regions in $U_C(c_1^{la})|_{x=L}$ and $U_C(\bar{c}_1)$, η_1^r shows wide negative valleys.

The right-shifted positive peaks in η_1^d and wide negative valleys in η_1^r (Fig. 5b) are all because of the deviations of $U_C(c_1^{la})|_{x=L}$ from $U_C(\bar{c}_1)$, which is induced by a non-uniform j_C (Fig. 3). To investigate this phenomenon in detail, additional simulations have been performed with j_C^u (Eq. (16)) and the results are shown in Fig. S6. In this particular case, the local average concentration is equal to the total average concentration, *i.e.* $c_1^{la} = \bar{c}_1$, which can be seen from the blue and gold curves in Fig. S6c. That makes $U_C(c_1^{la})|_{x=L} = U_C(\bar{c}_1)$, causing η_1^r equal to zero, and therefore no negative values are found in η_1^r. η_1^c is therefore in this case equal to η_1^d. From Fig. S6a it can be seen that the peaks in η_1^d ($= \eta_1^c$) appear at the same moment as the sloping regions in the OCV curve, *i.e.* without shifts to the right.

Fig. S7 decouples η_1^c (a) into η_1^d (b) and η_1^r (c) at various C-rates. Obviously, η_1^d increases with C-rate at the end of charging, obviously indicating larger concentration gradients within solid particles at higher C-rates. It can also be seen that the positive peaks in η_1^d continuously shift to the right with increasing C-rates. The negative valleys in η_1^r also become wider and more negative at higher C-rates. This effect is a consequence of j_C becoming more non-uniform at higher currents as revealed in Fig. 3. It is worth mentioning that the term 'solid Li concentration overpotential' in literature [23,25] frequently refers to the Li concentration diffusion overpotential in solid, *i.e.* to η_1^d rather than η_1^c in the present paper.

4.3. Kinetic overpotential

In the present model, the kinetic overpotential (η^{ct}) is equal to the difference between the charge-transfer overpotential at the CC and the LS interface, as given in Eq. (15.4). It should be noted that the charge-transfer overpotential at the CC interface is far more dominant in comparison to that at the Li metal interface.

Fig. 6a shows η^{ct} at various C-rates again with the OCV curve as reference. As expected, η^{ct} increases with applied current and apparent fluctuations can be seen for all C-rates. From Eq. (15.4) it can be derived that both $i_C^0|_{x=L}$ and $j_C|_{x=L}$ are responsible for the fluctuations because all other parameters are constant, and the charge-transfer overpotential of Li metal (at the LS interface) is negligibly small. It is also shown that $i_C^0|_{x=L}$ is inversely proportional to η^{ct}, while $j_C|_{x=L}$ is directly proportional to η^{ct} in Eq. (15.4). Note that both i_C^0 and j_C have a distribution across the electrode thickness, and only the values of i_C^0 and j_C at the CC interface ($i_C^0|_{x=L}$ and $j_C|_{x=L}$) influence η^{ct}. To reveal the dependency of η^{ct} on $i_C^0|_{x=L}$, simulations at 0.5C charging have been performed with a constant i_C^0 (Fig. S8). It can be seen that evident fluctuations emerge even though i_C^0 is constant (blue line in Fig. S8). These simulations demonstrate that the fluctuations in η^{ct} are not caused by i_C^0. However, high values of η^{ct} at the beginning and the end of charging disappear in the case of constant i_C^0. Such high values of η^{ct} with a non-constant i_C^0 (red line) are caused by the Li concentration in the solid, as can be seen from Eq. T8. At the beginning of delithiation, $c_1^s \approx c_1^{max}$ and therefore i_C^0 is low. At the end of operation, c_1^s approaches zero, again making i_C^0 small. In both cases η^{ct} is high because, according to Eq. (15.4), it is inversely proportional to i_C^0.

To reveal the relation between η^{ct} and $j_C|_{x=L}$, Fig. 6b shows η^{ct} with a non-uniform and uniform distribution of the reaction rate ($j_C|_{x=L}$ and $j_C^u|_{x=L}$) at 0.5C. The total distribution of j_C and j_C^u across the porous electrode is shown in Fig. 3c and Fig. S3c, respectively. In Fig. 6b, the simultaneous fluctuations of η^{ct} and $j_C|_{x=L}$ illustrate the high correlation between these two under a non-uniform condition, while $j_C^u|_{x=L}$ results in a smooth η^{ct}. Since we have already demonstrated that i_C^0 does not influence the fluctuations in η^{ct}, it can now be concluded that $j_C|_{x=L}$ is exclusively responsible for the fluctuations in η^{ct}. In addition, Fig. 6a shows that the peaks in η^{ct} move to the right with increasing C-rate. This feature is traced back to more non-uniform behavior of j_C at higher currents, resulting in the peaks in $j_C|_{x=L}$ moving to the higher values of transferred charge (see Fig. 3).

In general, a real electrode interface is more complex than in the presented model because it includes, for example, a solid electrolyte interface (SEI) surface film and an electrical double layer. These additional factors may cause additional overpotentials. The presence of an electrical double layer has a strong influence on the transient state, especially at the beginning and end of (dis)charging [54,55].

4.4. Ohmic overpotential

The ohmic overpotential includes the electrolyte ohmic overpotential (η_2^Ω), and the electrode ohmic overpotential (η_1^Ω) caused by the SEI film and other contact electrode resistances [56,57]. In the presented model, η_1^Ω is considered constant during constant-current (dis)charging. Since this work focuses on disclosing the dynamic behavior of the overpotential, only η_2^Ω will be discussed further. As shown in Eq. (15.6), the current distribution in the electrolyte (i_2) and the effective ionic conductivity of the electrolyte (κ_m and κ_C) determine η_2^Ω for a given set of parameters. According to the transformation of Eq. T13, i_2 can be obtained by the integral of j_C, indicating that j_C is involved in determining η_2^Ω implicitly.

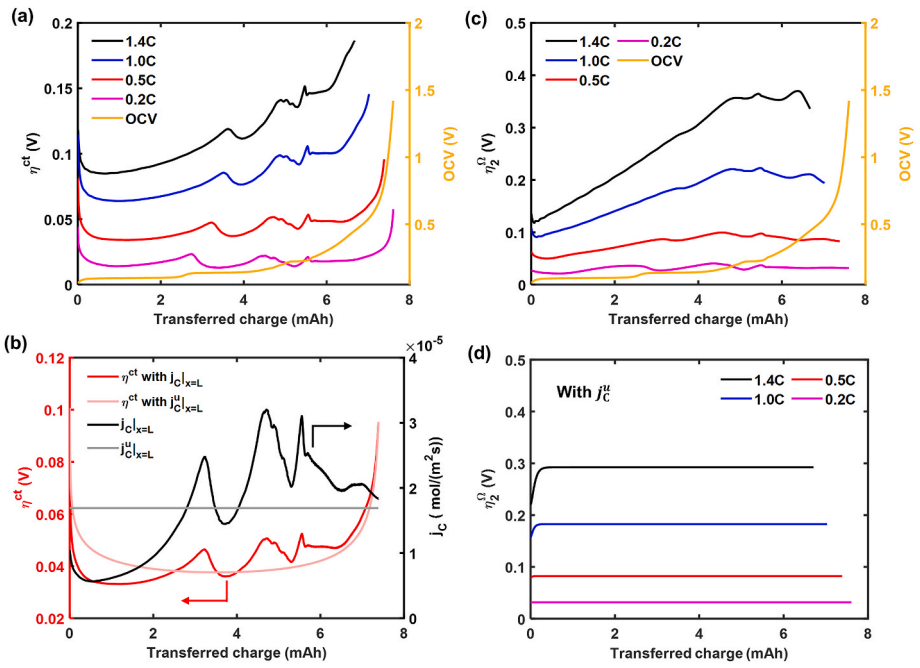

Fig. 6. (a) Kinetic overpotential (η^{ct}) at various C-rates and OCV curve and (b) comparison of η^{ct} with a uniform and non-uniform reaction-rate distribution ($j_C|_{x=L}$ and $j_C^u|_{x=L}$) at 0.5 C-rate. (c) Electrolyte ohmic overpotential (η_2^{Ω}) at different C-rates and OCV, and (d) η_2^{Ω} at different C-rates with j_C^u.

Fig. 6c shows the simulations of η_2^{Ω} at different C-rates. For all C-rates, η_2^{Ω} fluctuates with the transferred charge. To investigate the cause of these fluctuations, κ and i_2 are analyzed. κ is dependent on the electrolyte concentration (Table 2). Fig. S9 shows simulation results of η_2^{Ω}, in which κ is constant. In this case, η_2^{Ω} still increases and fluctuates with the transferred charge. Fig. 6d shows η_2^{Ω} for the case of a j_C^u (Eq. (16)) and a concentration-dependent κ. In this case, η_2^{Ω} increases sharply at the very beginning of charging, which is a result of the concentration gradient formation in the electrolyte (Fig. 4d), and remains more or less constant afterwards. Therefore, the fluctuation of η_2^{Ω} is attributed to a changing i_2 during charging, which is influenced by the non-uniform j_C. Note that η_2^{Ω} increases with C-rate, mainly because the value of i_2 increases with increasing current.

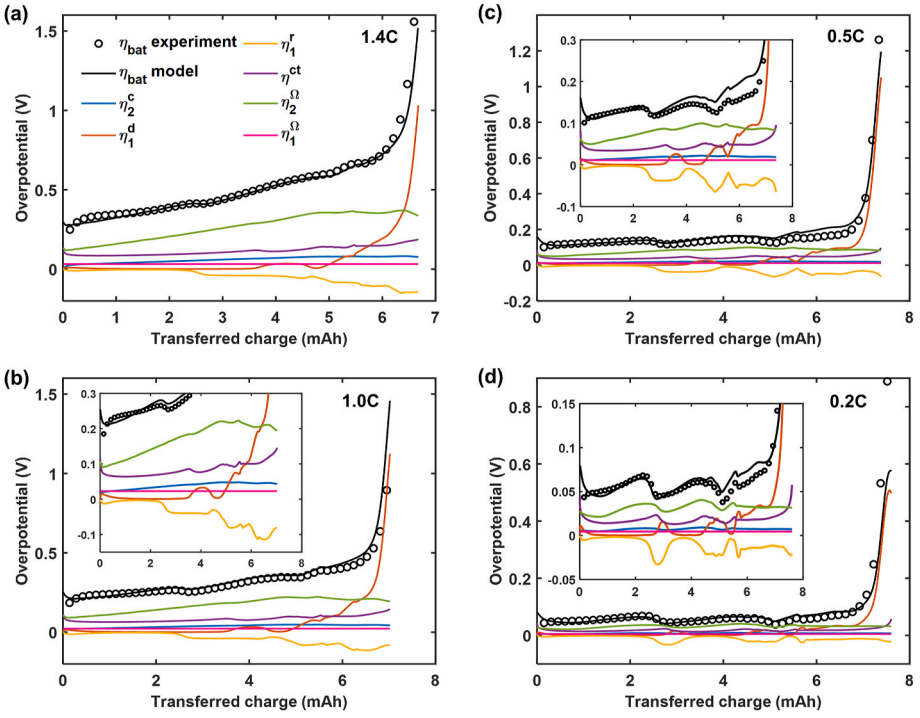

Fig. 7. An overview of the various overpotentials as a function of transferred charge at (a) 1.4C, (b) 1C, (c) 0.5C, and (d) 0.2C. The solid lines represent model simulations, and the circles represent experimental data. The insets in (b–d) show partial enlargements of the figures.

4.5. Total overpotential

Fig. 7 shows the comparison of all overpotential components at various C-rates, which have been explained in detail in Section 4.1-4.4. In general, η_2^{Ω} is the major contributor to the total overpotential during charging. η^{ct} take the second contribution. η_1^d increases rapidly at the end of charging and therefore contributes significantly in that region. η_1^r is negative and small in magnitude, mainly responsible for the fluctuations in the total overpotential. The contributions from η_2^c and η_1^{Ω} are negligibly small.

The total overpotential shows some valleys near the sloping regions of the OCV (Figs. 2b and 7). η_2^c, η_1^d, η^{ct} and η_2^{Ω} (Figs. 4–7) all show minor peaks or fluctuations near these OCV regions, therefore they do not considerably contribute to the valleys in total overpotential. In contrast, η_1^r shows negative valleys near the sloping regions in OCV and is mostly responsible for the valleys in total overpotential, which cause the disappearance of the sloping regions for the voltage curves at higher currents. It has been concluded in Section 4.2 that η_1^r is largely affected by the non-uniformity of j_C, which makes that the delithiation of particles near the CC interface is delaying particles near the SC interface. Larger non-uniformity of j_C at higher currents causes much delay of delithiation among particles and subsequently generates wider and more negative valleys in η_1^r (Fig. 5 and Fig. S6), which lead to the disappearance of distinct plateaus and sloping regions in the voltage curves.

Fig. 8 shows a summary of the complex interactions between the various overpotential components in the P2D model. Four major overpotential components, shown by the green areas, are coupled together through j_C (yellow rectangle). η^{ct} is expressed as the charge-transfer process at the LS and CC interfaces and is mainly determined by j_C at the CC interface. Moreover, η^{ct} is also dependent on the electrolyte concentration (c_2) and Li concentration in solid (c_1) through the exchange current density. η_2^c depends on the electrolyte concentration (c_2), which is considerably governed by j_C. η_1^c is the summation of η_1^d and η_1^r, caused by Li diffusion in the solid and j_C, respectively. The ohmic overpotential contains the electrolyte ohmic (η_2^{Ω}) and other pure electrode ohmic overpotentials (η_1^{Ω}). η_2^{Ω} shows a strong dependency on the electrolyte properties and the current distribution, which is the integral of j_C. In short, η_2^c, η_1^d, η_1^r, η^{ct} and η_2^{Ω} are all influenced by j_C and are coupled together through j_C. j_C is governed by a set of physical/electrochemical battery parameters, which are shown in the blue oval. In addition, c_1 and c_2, shown in the orange rectangles, also influences j_C.

Reducing the overpotential in batteries is essential for the design and application of high-quality and high-performance LIBs. Based on the analyses in the present paper, several suggestions can be offered to reduce the total overpotential. To reduce η_2^{Ω}, which is found to be the highest overpotential component in this work, more optimized designs of electrolytes, porous electrodes, and separators have to be considered. An electrolyte with high ionic conductivity is always helpful. Optimizing the porosity and tortuosity of the porous electrodes and separators would also lead to lower overpotentials. η_2^c will be decreased by improving the transport parameters of the electrolyte and optimizing the designs of porous electrodes and separators. Decreasing the particle size will decrease the diffusion length and therefore reduce η_1^d. η_1^r is negative for delithiation and is largely influenced by the reaction-rate distribution. However, one should not strive for even more negative η_1^r values at the expense of η_1^d, because only the sum of these two components contributes to the total overvoltage. The ideal case is that the reaction-rate distribution is uniform, inducing η_1^r to approach 0. η^{ct} can be reduced by increasing the exchange current density, which can be improved by, for example, surface modifications. In addition, several other factors can be considered for further optimization, such as specific battery operating conditions, for example, high-energy or high-power applications.

5. Conclusions

The present paper mathematically describes the overpotential of a C-based electrode/Li battery in the porous electrode model framework. Four mathematically defined overpotential terms, including the electrolyte concentration overpotential, the Li concentration overpotential in the solid, the kinetic overpotential, and the electrolyte ohmic overpotential, are derived and studied. The overpotential behavior as a function of the applied current, the reaction-rate distribution, and other model variables has been illustrated. The electrolyte concentration overpotential is determined by the electrolyte concentration gradient across the battery, which is influenced by the reaction-rate distribution. The Li concentration overpotential in the solid is decoupled into the Li concentration overpotential within a single particle and among all particles. These two terms are induced by the Li diffusion within one particle and the non-uniform reaction-rate distribution, respectively. The kinetic overpotential and the electrolyte ohmic overpotential are also (in)directly influenced by the reaction-rate distribution.

The four overpotential terms are coupled and show dynamic fluctuations during operation due to the dynamic changes of the reaction-rate distribution. Specifically, the disappearance of the phase-change information in the voltage curve of the graphite-based porous electrode/Li battery under moderate and high C-rates is ascribed to the Li concentration overpotential among solid particles, resulting from the

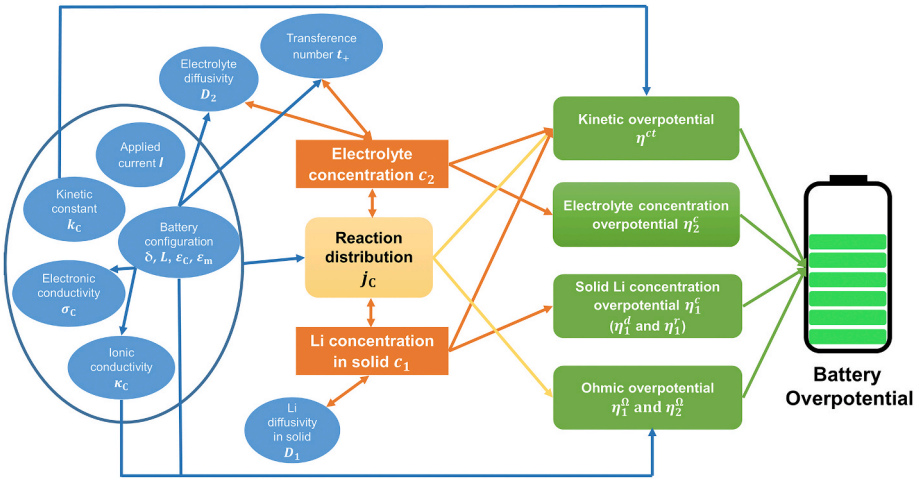

Fig. 8. The relationships between the battery parameters and various overpotentials. The one-way arrow represents that the variables at the beginning of the arrow influences the variables at the end of the arrow. The double-sided arrow denotes that the variables at both sides of the arrow influence each other.

non-uniform reaction-rate distribution. The conclusions drawn in this paper for charging also hold for discharging (lithiation). The four overpotential components are always present and play an important role in determining the voltage curves and storage capacities. In addition, the approach used in this work can be straightforwardly extended for batteries with two porous electrodes.

CRediT authorship contribution statement

Zhiqiang Chen: Conceptualization, Software, Validation, Writing – original draft. **Dmitri L. Danilov:** Conceptualization, Software, Supervision, Writing – review & editing. **Luc H.J. Raijmakers:** Validation, Writing – review & editing, Battery tests and validation, Review & editing. **Kudakwashe Chayambuka:** Software. **Ming Jiang:** Validation, Battery tests and validation. **Lei Zhou:** Validation, Battery tests and validation. **Jiang Zhou:** Providing testing materials. **Rüdiger-A. Eichel:** Project administration. **Peter H.L. Notten:** Conceptualization, Supervision, Writing – review & editing.

Declaration of competing interest

The authors declare that they have no known competing financial interests or personal relationships that could have appeared to influence the work reported in this paper.

Acknowledgements

Mr. Z. Chen, Mrs. M. Jiang and Dr. L. Zhou gratefully acknowledge fellowships support by the China Scholarship Council. Dr. D.L. Danilov and Dr. L.H.J. Raijmakers appreciate support from the Federal Ministry for Economic Affairs and Energy, Germany within the project LimeSI, grant number 03ETE019E. The authors also acknowledge Mr. Q. Zhang from Fundamental Electrochemistry (IEK-9), Forschungszentrum Jülich, for the help of measurements of SEM and EDX.

Appendix A. Supplementary data

Supplementary data to this article can be found online at https://doi.org/10.1016/j.jpowsour.2021.230345.

Nomenclature

a	Specific interfacial area of the C-based electrode (m^{-1})
$brugg_C$, $brugg_m$	Bruggeman coefficient in the C-based electrode and separator membrane region (−)
c_1	Li concentration in the solid particle (mol m^{-3})
c_1^s	Surface Li concentration of the solid particle (mol m^{-3})
c_1^{max}	Maximum Li concentration in the solid particle (mol m^{-3})
c_1^{la}	Local average Li concentration in the solid particle (mol m^{-3})
$\bar{c}_1$	Total average Li concentration in the solid particle (mol m^{-3})
c_2	Electrolyte concentration (mol m^{-3})
D_2	Diffusion coefficient of the electrolyte (m^2 s^{-1})
D_2^C, D_2^m	Effective diffusion coefficient of the electrolyte in the C-based electrode and separator membrane region (m^2 s^{-1}) $D_2^C = D_2 \varepsilon_C^{brugg_C}$, $D_2^m = D_2 \varepsilon_m^{brugg_m}$
D_1	Diffusion coefficient of Li-ions in the solid particle (m^2 s^{-1})
F	Faraday's constant, 96487 (C mol^{-1})
i_1	Current density in the solid (A m^{-2})
i_2	Current density in the electrolyte (A m^{-2})
I	Applied current density (A m^{-2})
i_C^0	Exchange current density of the C-based electrode (A m^{-2})
i_{Li}^0	Exchange current density of the Li metal (A m^{-2})
j_C	Reaction-rate distribution of the C-based electrode (mol m^{-2} s^{-1})
j_C^u	Uniform reaction-rate distribution of the C-based electrode (mol $m^{-2}s^{-1}$)
k_C	Kinetic constant of the C-based electrode (−)
L	Thickness of the cell (m)
r	Radius vector of the C-based particle (m)
R	Gas constant, 8.314 (J mol^{-1} K^{-1})
R_f	Ohmic resistance (Ω m^2)
R_1	Radius of the solid particle (m)
t	Time (s)
t_+	Transference number of Li-ions in the electrolyte (−)
T	Temperature (K)
U_C	Equilibrium potential of C-based electrode (V)
α, α_{Li}	Charge-transfer coefficients (−)
δ	Thickness of the separator (m)
ε_m, ε_C, ε_f	Porosity of the separator membrane, the C-based electrode, and conductive fillings (−)
η_C^{ct}	Charge-transfer overpotential of the C-based electrode (V)
Φ_1	Potential in the solid (V)
Φ_2	Potential in the solution (V)
κ	Ionic conductivity of the electrolyte (S m^{-1})
σ	Electronic conductivity of the solid (S m^{-1})
$\kappa_C\kappa_m$	Effective ionic conductivity of the electrolyte in the C-based electrode and separator membrane region (S m^{-1}) .$\kappa_C = \kappa \varepsilon_C^{brugg_C}$., κ_m =

$\kappa\varepsilon_m^{brugg_m}$

σ_C Effective electronic conductivity of the C-based electrode (S m^{-1}) $\sigma_C = \sigma(1 - \varepsilon_C)$

η_1^c Li concentration overpotential in electrode solid particles (V)

η_1^d the Li overpotential in the radial direction within a single particle induced by diffusion, as one part of η_1^c (V)

η_1^r the Li concentration overpotential among all particles induced by the non-uniform reaction, as one part of η_1^c (V)

η_2^c Electrolyte concentration overpotential component (V)

η^{ct} Charge-transfer overpotential component (V)

η_2^Ω Electrolyte ohmic overpotential component (V)

η_1^Ω Electrode ohmic overpotential component (V)

Subscripts

1 Properties in the solid phase of the electrode

2 Properties in the electrolyte phase

C Properties of the C-based porous electrode

Li Properties of metallic Li

Superscripts

s Surface

la Local average

max maximum

References

[1] R. Schmuch, R. Wagner, G. Hörpel, T. Placke, M. Winter, Performance and cost of materials for lithium-based rechargeable automotive batteries, Nat. Energy 3 (2018) 267–278.

[2] L.H.J. Raijmakers, D.L. Danilov, R.A. Eichel, P.H.L. Notten, A review on various temperature-indication methods for Li-ion batteries, Appl. Energy 240 (2019) 918–945.

[3] A.J. Bard, L.R. Faulkner, Electrochemical Methods Fundamentals and Applications, John Wiley & Sons, 1980.

[4] W. Waag, D.U. Sauer, Adaptive estimation of the electromotive force of the lithium-ion battery after current interruption for an accurate state-of-charge and capacity determination, Appl. Energy 111 (2013) 416–427.

[5] D.M. Bernardi, J.-Y. Go, Analysis of pulse and relaxation behavior in lithium-ion batteries, J. Power Sources 196 (2011) 412–427.

[6] L. Pei, T. Wang, R. Lu, C. Zhu, Development of a voltage relaxation model for rapid open-circuit voltage prediction in lithium-ion batteries, J. Power Sources 253 (2014) 412–418.

[7] A. Barai, K. Uddin, W.D. Widanage, A. McGordon, P. Jennings, A study of the influence of measurement timescale on internal resistance characterisation methodologies for lithium-ion cells, Sci. Rep. 8 (2018) 21.

[8] D. Andre, M. Meiler, K. Steiner, H. Walz, T. Soczka-Guth, D.U. Sauer, Characterization of high-power lithium-ion batteries by electrochemical impedance spectroscopy. II: Modelling, J. Power Sources 196 (2011) 5349–5356.

[9] A.K. Hjelm, G. Lindbergh, Experimental and theoretical analysis of LiMn2O4 cathodes for usein rechargeable lithium batteries by electrochemical impedancespectroscopy (EIS), Electrochim. Acta 47 (2002) 1747–1759.

[10] K.J. Vetter, Electrochemical Kinetics: Theoretical Aspects, Academic Press, 1967.

[11] K. Smith, C.-Y. Wang, Solid-state diffusion limitations on pulse operation of a lithium ion cell for hybrid electric vehicles, J. Power Sources 161 (2006) 628–639.

[12] Y. Li, F. El Gabaly, T.R. Ferguson, R.B. Smith, N.C. Bartelt, J.D. Sugar, K.R. Fenton, D.A. Cogswell, A.L. Kilcoyne, T. Tyliszczak, M.Z. Bazant, W.C. Chueh, Current-induced transition from particle-by-particle to concurrent intercalation in phase-separating battery electrodes, Nat. Mater. 13 (2014) 1149–1156.

[13] J. Newman, K.E. Thomas-Alyea, Electrochemical Systems, John Wiley & Sons, 2004.

[14] K. Onda, T. Ohshima, M. Nakayama, K. Fukuda, T. Araki, Thermal behavior of small lithium-ion battery during rapid charge and discharge cycles, J. Power Sources 158 (2006) 535–542.

[15] V.J. Ovejas, A. Cuadras, State of charge dependency of the overvoltage generated in commercial Li-ion cells, J. Power Sources 418 (2019) 176–185.

[16] S.E. Li, B. Wang, H. Peng, X. Hu, An electrochemistry-based impedance model for lithium-ion batteries, J. Power Sources 258 (2014) 9–18.

[17] Y. Zhang, C.-Y. Wang, X. Tang, Cycling degradation of an automotive LiFePO4 lithium-ion battery, J. Power Sources 196 (2011) 1513–1520.

[18] E. Prada, D. Di Domenico, Y. Creff, J. Bernard, V. Sauvant-Moynot, F. Huet, Simplified electrochemical and thermal model of LiFePO4-graphite Li-ion batteries for fast charge applications, J. Electrochem. Soc. 159 (2012) A1508–A1519.

[19] V. Srinivasan, J. Newman, Discharge model for the lithium iron-phosphate electrode, J. Electrochem. Soc. 151 (2004) A1517.

[20] A. Nyman, T.G. Zavalis, R. Rlger, M. Behem, G. Lindbergh, Analysis of the polarization in a Li-ion battery cell by numerical simulations, J. Electrochem. Soc. 157 (2010) A1236–A1246.

[21] F. Yang, Y. Qiao, B. Gao, P. Duan, Y. Zhu, Investigation on Li-ion battery charging polarization characteristics and influence factors, Ionics 22 (2016) 1603–1610.

[22] R. Chandrasekaran, Quantification of contributions to the cell overpotential during galvanostatic discharge of a lithium-ion cell, J. Power Sources 262 (2014) 501–513.

[23] P.E.d. Jongh, P.H.L. Notten, Effect of current pulses on lithium intercalation batteries, Solid State Ionics 148 (2002) 259–268.

[24] M. Doyle, J. Newman, Analysis of capacity–rate data for lithium batteries using simplified models of the discharge process, J. Appl. Electrochem. 27 (1997) 846–856.

[25] S. Hou, T. Gao, X. Li, C. Wang, Operando probing ion and electron transport in porous electrodes, Nano Energy 67 (2020) 104254.

[26] D. Danilov, P.H.L. Notten, Mathematical modelling of ionic transport in the electrolyte of Li-ion batteries, Electrochim. Acta 53 (2008) 5569–5578.

[27] L.H.J. Raijmakers, D.L. Danilov, R.A. Eichel, P.H.L. Notten, An advanced all-solid-state Li-ion battery model, Electrochim. Acta 330 (2020) 135147.

[28] H.J. Bergveld, W.S. Kruijt, P.H.L. Notten, Battery Management Systems: Design by Modelling, Kluwer Academic Publishers, 2002.

[29] D. Danilov, R.A.H. Niessen, P.H.L. Notten, Modeling all-solid-state Li-ion batteries, J. Electrochem. Soc. 158 (2011) A215.

[30] N. Kazemi, D.L. Danilov, L. Haverkate, N.J. Dudney, S. Unnikrishnan, P.H. L. Notten, Modeling of all-solid-state thin-film Li-ion batteries: accuracy improvement, Solid State Ionics 334 (2019) 111–116.

[31] M. Doyle, T.F. Fuller, J. Newman, Modeling of galvanostatic charge and discharge of the lithium/polymer/insertion cell, J. Electrochem. Soc. 140 (1993) 1526–1533.

[32] T.F. Fuller, M. Doyle, J. Newman, Simulation and optimization of the dual lithium ion insertion cell, J. Electrochem. Soc. 141 (1994) 1–10.

[33] G. Zhang, C.E. Shaffer, C.-Y. Wang, C.D. Rahn, In-Situ measurement of current distribution in a Li-ion cell, J. Electrochem. Soc. 160 (2013) A610–A615.

[34] S.H. Ng, F. La Mantia, P. Novak, A multiple working electrode for electrochemical cells: a tool for current density distribution studies, Angew. Chem. Int. Ed. 48 (2009) 528–532.

[35] Y. Zhang, Z. Yang, C. Tian, Probing and quantifying cathode charge heterogeneity in Li ion batteries, J. Mater. Chem. A 7 (2019) 23628–23661.

[36] J. Newman, C.W. Tobias, Theoretical analysis of current distribution in porous electrodes, J. Electrochem. Soc. 109 (1962) 1183–1191.

[37] J. Newman, W. Tiedemann, Porous-electrode theory with battery applications, AIChE J. 21 (1975) 25–41.

[38] Z. Chen, D.L. Danilov, R.-A. Eichel, P.H.L. Notten, On the reaction rate distribution in porous electrodes, Electrochem. Commun. 121 (2020) 106865.

[39] J. Sturm, A. Rheinfeld, I. Zilberman, F.B. Spingler, S. Kosch, F. Frie, A. Jossen, Modeling and simulation of inhomogeneities in a 18650 nickel-rich, silicon-graphite lithium-ion cell during fast charging, J. Power Sources 412 (2019) 204–223.

[40] K.H. Chen, V. Goel, M.J. Namkoong, M. Wied, S. Müller, V. Wood, J. Sakamoto, K. Thornton, N.P. Dasgupta, Enabling 6C fast charging of Li-ion batteries with graphite/hard carbon hybrid anodes, Adv. Energy Mater. (2020) 2003336.

[41] S. Jung, Mathematical model of lithium-ion batteries with blended-electrode system, J. Power Sources 264 (2014) 184–194.

[42] X. Li, S.-Y. Choe, W.T. Joe, A reduced order electrochemical and thermal model for a pouch type lithium ion polymer battery with $LiNi_xMn_yCo_{1-x-y}O_2/LiFePO_4$ blended cathode, J. Power Sources 294 (2015) 545–555.

[43] T.F. Fuller, M. Doyle, J. Newman, Relaxation phenomena in lithium-ion-insertion cells, J. Electrochem. Soc. 141 (1994) 982–990.

[44] J.R. Dahn, R. Fong, M.J. Spoon, Suppression of staging in lithium-intercalated carbon by disorder in the host, Phys. Rev. B 42 (1990) 6424–6432.

[45] J.R. Dahn, Phase diagram ofLixC6, Phys. Rev. B 44 (1991) 9170–9177.

[46] S. Malifarge, B. Delobel, C. Delacourt, Experimental and modeling analysis of graphite electrodes with various thicknesses and porosities for high-energy-density Li-ion batteries, J. Electrochem. Soc. 165 (2018) A1275–A1287.
[47] T.D. Tran, J.H. Feikert, R.W. Pekala, Rate effect on lithium-ion graphite electrode performance, J. Appl. Electrochem. 26 (1996) 1161–1167.
[48] D.D. Domenico, G. Fiengo, A. Stefanopoulou, Lithium-Ion battery State of Charge estimation with a Kalman Filter based on a electrochemical model, in: 17th IEEE International Conference on Control Applications, 2008, pp. 702–707.
[49] Z. Chen, D.L. Danilov, R.-A. Eichel, P.H.L. Notten, Electrolyte Concentration Waves in Graphite-based Porous Electrode/Li Cell, In progress.
[50] S.J. Harris, A. Timmons, D.R. Baker, C. Monroe, Direct in situ measurements of Li transport in Li-ion battery negative electrodes, Chem. Phys. Lett. 485 (2010) 265–274.
[51] S.A. Krachkovskiy, J.M. Foster, J.D. Bazak, B.J. Balcom, G.R. Goward, Operando mapping of Li concentration profiles and phase transformations in graphite electrodes by magnetic resonance imaging and nuclear magnetic resonance spectroscopy, J. Phys. Chem. C 122 (2018) 21784–21791.
[52] H. Murayama, K. Kitada, K. Fukuda, A. Mitsui, K. Ohara, H. Arai, Y. Uchimoto, Z. Ogumi, E. Matsubara, Spectroscopic X-ray diffraction for microfocus inspection of Li-ion batteries, J. Phys. Chem. C 118 (2014) 20750–20755.
[53] F. Rittweger, C. Modrzynski, V. Roscher, D.L. Danilov, P.H.L. Notten, K.-R. Riemschneider, Investigation of charge carrier dynamics in positive lithium-ion battery electrodes via optical in situ observation, J. Power Sources 482 (2021) 228943.
[54] I.J. Ong, J. Newman, Double-layer capacitance in a dual lithium ion insertion cell, J. Electrochem. Soc. 146 (1999) 4360–4367.
[55] N. Legrand, S. Raël, B. Knosp, M. Hinaje, P. Desprez, F. Lapicque, Including double-layer capacitance in lithium-ion battery mathematical models, J. Power Sources 251 (2014) 370–378.
[56] J. Li, E. Murphy, J. Winnick, P.A. Kohl, Studies on the cycle life of commercial lithium ion batteries during rapid charge–discharge cycling, J. Power Sources 102 (2001) 294–301.
[57] S.J. An, J. Li, Z. Du, C. Daniel, D.L. Wood, Fast formation cycling for lithium ion batteries, J. Power Sources 342 (2017) 846–852.